Physics of Fluids ARTICLE pubs.aip.org/aip/pof

On the slip correction for micro- and nano-particles in gas flows

Cite as: Phys. Fluids **38**, 012015 (2026); doi: 10.1063/5.0309021
Submitted: 25 October 2025 · Accepted: 5 January 2026 ·
Published Online: 23 January 2026

Ning-Ning Liu,[1] Bing-Yang Cao,[1,a)] and Sergei S. Sazhin[2,3,a)]

AFFILIATIONS

[1]Key Laboratory for Thermal Science and Power Engineering of the Ministry of Education, Department of Engineering Mechanics, Tsinghua University, Beijing 100084, China
[2]National Research Tomsk Polytechnic University, Tomsk, Russian Federation
[3]Kutateladze Institute of Thermophysics, Siberian Branch of the Russian Academy of Sciences, Novosibirsk, Russian Federation

[a)]**Authors to whom correspondence should be addressed:** caoby@mail.tsinghua.edu.cn and sergei.sazhin@icloud.com

ABSTRACT

The effects of Knudsen numbers (Kn), particle sizes, their relative velocities, and particle and gas properties on the drag force acting on micro- and nano-particles, moving in a gas, are investigated using the molecular dynamics approach. The slip correction factor C and the slip parameter A are shown to depend not only on Kn, as commonly assumed, but also on the physical properties of the gases and particles. Quantitative analysis of the ratio between local (near the particle surface) and ambient gas number densities showed that increased gas–particle interactions at micro- and nano-scales lead to an increase in the local gas number density, which leads to an increase in the drag force. A comprehensive potential depth parameter ε_{ggp} is introduced to take into account both gas–particle and gas–gas interactions. This parameter allowed us to provide a unified framework for interpreting slip correction factor behavior for different particle–gas combinations. A universal predictive approximation of the slip parameter is suggested as a function of ε_{ggp} and Kn. The prediction of this approximation is shown to be in good agreement with experimental data referring to the drag forces experienced by polystyrene latex particles in nitrogen at $Kn > 10$.

I. INTRODUCTION

The drag force experienced by fine particles moving in a gas is a critical factor that determines their motion characteristics, sedimentation behavior, and transport processes. It is of significant importance in numerous fields such as microfluidic technology, atmospheric science, and nano-particle synthesis.[1–3] Currently, classical hydrodynamic drag models are widely used to describe particle motion in fluids. Under conditions with low Reynolds numbers ($Re < 5$), the aerodynamic drag force F_d can typically be calculated using the classical Stokes law

$$F_d = 6\pi\mu RU, \tag{1}$$

where μ is the gas dynamic viscosity (Pa s), R is the radius of the particle (m), and U is the relative velocity between the particle and the gas (m/s). This model is based on the continuum assumption and is suitable for estimating the drag force experienced by relatively large particles moving in dense gas environments. Significant deviations arise between the predictions of Expression (1) and the actual drag force acting on the particle when the particle radius (R) is comparable to or less than the mean free path (λ) of gas molecules (the Knudsen number, $Kn = \lambda/R$, is of the order of or greater than 1). With increasing gas rarefaction, especially in the slip flow and free-molecular flow regimes, the drag model described by Expression (1) must be corrected to fully account for the effects of non-continuum phenomena.

Correction for the drag force acting on these particles was introduced by Cunningham[4] in the form of a slip correction factor C. This correction factor considered the slip effect of gas molecules at the particle surface, and led to the following generalization of Expression (1):

$$F_d = \frac{6\pi\mu RU}{C}. \tag{2}$$

Cunningham[4] proposed a linear relationship between C and Kn: $C(Kn) = 1 + A{\cdot}Kn$, where A is the slip parameter, initially treated as a constant. However, this model is only applicable to the slip regime where $Kn < 1$. To extend its applicability across a wider range of Kn, particularly in the transition and free-molecular flow regimes, the dependence of A on Kn was taken into account. Using experimental data, a unified drag correction expression, valid for the entire Kn range, was suggested as follows:[5,6]

$$F_d = \frac{6\pi\mu RU}{1 + Kn\left[\alpha + \beta e^{\left(-\frac{\gamma}{Kn}\right)}\right]}, \tag{3}$$

where the coefficients α, β, and γ are determined by fitting the experimental data. Formula (3) implies that

$$A = \alpha + \beta e^{\left(-\frac{\gamma}{Kn}\right)}. \tag{4}$$

Formula (3) has been validated by data inferred from numerous experimental studies.[7–11] A is commonly known as the slip parameter.[5]

Although the fitted values of α and β varied between different experiments, $\alpha + \beta$ fell mostly within the range 1.30–1.65. Some studies reported values of this sum as low as 1.03 and as high as 1.88. However, all studies consistently indicated that the overall trend of how the parameter A changes with Kn remains the same.

Note that these findings have sparked some controversy within the academic community, particularly regarding the conclusion that $\alpha + \beta$ remains largely independent of gas composition and particle surface properties. The experimental results of Hutchins *et al.*[9] revealed a discrepancy of up to 8 % between solid particles and oil droplets when $0.09 \leq \mathrm{Kn} \leq 18$. Experiments by Jung *et al.*[12] demonstrated that gas molecular slip is strongly influenced by the properties of the particle material, with the proportion of diffusive reflection of gas molecules on the surfaces of polystyrene latex particles being 12 % lower than that on the surfaces of gold. In the limit $Kn \gg 1$, Formula (3) is consistent with the result derived by Epstein[13] based on gas kinetic theory, i.e., $\alpha + \beta \approx 2.25/\delta$ (see Refs. 7 and 12), where δ is the reflection coefficient, which depends on the type of collision between the surface and the gas molecules, and its value is typically taken as 1.4. Expression (3), often referred to as Millikan's fall law, is still commonly used for the quantitative estimation and prediction of particle drag, with the parameters α, β, and γ adjusted empirically based on observations.

However, recent research on aerodynamic drag correction for micro- and nano-particles has revealed significant discrepancies between the predictions of Millikan's fall law and experimental data for $Kn < 10$ (see Ref. 14). Millikan's law predicts that A gradually increases from about 1.2 to about 1.6 as Kn increases in the range 0.1–100, whereas the experimental results obtained by Jakobsen *et al.*[14] show that A decreases from about 3 to around 1.7 as Kn increases in the range 0.32–183. Although the values of A predicted by Formula (4) are consistent with observations by Jakobsen *et al.* for $Kn > 10$, a significant deviation between predicted and observed A under low Kn conditions still raises suspicions that unidentified systematic errors could affect modeling results.

Furthermore, when analyzing the drag correction in the $Kn > 1$ regime, Epstein[13] assumed that collisions between gas molecules and particles are elastic and that the gas molecule number density near the particle is equal to that in the far-field environment. However, on the micro- and nano-scales, the assumption of elastic collisions often no longer holds, and effects due to non-elastic collisions (van der Waals forces) must be considered.[15–17] On the other hand, if the interaction between gas and solid molecules is strong, some gas molecules can be captured by the particle surface, leading to a local gas molecule number density (N_{wall}) that is higher than in a far-field environment (N_{env}). This effect can lead to a significant increase in drag force compared to theoretically predicted results that ignore it.[13] Consequently, it will also differ from the value predicted by Formula (3) in the limit $\mathrm{Kn} \gg 1$ (see Ref. 18).

The discrepancy between the predictions of Formula (3) and the experimental data indicates that the assumptions of the model regarding gas–particle collision behavior are not applicable for the analysis of real-life experiments. The reflection mechanism of gas molecules at the surface of the particle, the energy transfer process during collisions, and the influences arising from material properties can vary significantly depending on the specific gas–particle system.

Molecular dynamics (MD) methods, which track atomic trajectories by directly solving Newton's equations of motion, can accurately reveal the dynamic evolution of microscopic systems and have emerged as a powerful tool for investigating the behavior of micro- and nano-particles in rarefied gases. In recent years, this technique has been successfully applied to the detailed analysis of nano-particle motion across the slip to free-molecular flow regimes. Li and Wang[19] employing a nitrogen-silver nano-particle model system, systematically explored gas–particle scattering behavior, elucidating the origin of diffuse reflection and the transition to specular reflection dependent on particle size and gas–particle binding energy. Jin *et al.*[20] utilized MD simulations to investigate the Brownian force on nano-particles, revealing that it exhibits a preferential frequency rather than the white noise previously assumed. Furthermore, Liu *et al.*,[18] using a copper-argon model system, studied the drag characteristics of nano-particles in the transition regime. Their results demonstrated that when the gas–particle interaction is strong, the simulated drag force can be 10%–20% higher than the drag force value in the transition regime predicted by Li and Wang.[21] The latter value was approached when the gas–particle interaction weakened.

Although these contributions have advanced our understanding of the drag correction at micro- and nano-scales, significant limitations remain. Publications on this topic have predominantly focused on single, specific gas–solid material combinations. An understanding of the universal mechanism by which different intermolecular potentials influence the drag correction is still lacking. The studies by Li *et al.*[19] and Jin *et al.*[20] did not focus directly on drag correction, but were more concerned with the fundamental physics of force mechanisms. The study by Liu *et al.* focused on nano-particles with radii smaller than 1.45 nm, elucidating the mechanism by which the gas–solid coupling strength modulates the drag force through its control over gas adsorption and the consequent change in the particle's effective diameter.[18] Their results demonstrate that, under weak coupling conditions, the adsorption of gas molecules on the particle surface is limited, leading to a negligible change in its effective diameter. As a result, the simulated drag force agrees well with the theoretical results presented in Ref. 21, which do not account for the effect of gas molecule adsorption on the effective particle size. In contrast, when the coupling strength is increased to a higher level, a pronounced adsorption layer of gas molecules forms (typically with a thickness below 1 nm). This layer effectively increases the hydrodynamic radius of the particle, ultimately resulting in a significant enhancement of the drag force experienced. However, for larger micro- and nano-particles, the influence of the surface adsorption layer is generally negligible. In this case, the fundamental interaction between gas and particle atoms/molecules becomes the key factor governing the drag correction. This effect has not yet been thoroughly investigated to the best of our knowledge.

The results of our study are expected to have various engineering applications, as accurate predictions of particle deposition, dispersion, and coagulation are highly dependent on reliable drag models.[22] Their

application to pollutant transport and inhaled drug delivery,[23,24] chemical vapor deposition and flame spray pyrolysis,[25–27] nano-particle synthesis,[28] and pneumatic lenses used for particle manipulation[29,30] is also expected. Traditional models often assume a universal slip correction factor for all particles, ignoring material-specific effects. However, as will be demonstrated in this study, the slip correction factor is highly sensitive to the properties of the particles and gas, and this needs to be considered in the modeling process.

II. NUMERICAL SIMULATION

A. Simulation model

A geometry used for molecular dynamics (MD) simulation of the motion of micro- or nano-particles in a gas flow is schematically presented in Fig. 1.

In our model, a micro- or nano-particle is fixed at the center of the simulation box, and gas molecules flow at a constant velocity in the x direction. Gas–solid and gas–liquid collision processes were investigated between solid silver (Ag) or gold (Au) particles, or water droplets, and three types of gases [nitrogen (N_2), helium (He), and argon (Ar)]. The Ag and Au particles were formed from face-centered cubic (FCC) crystals. The water droplet was constructed as a spherical subset extracted from a pre-equilibrated bulk water system. The bulk water, with an initial density of 1 g/cm^3, was composed of water molecules arranged on an FCC lattice within a cubic simulation box.

Given the large ratio between the diameter of the particle and the molecular diameter of the gas, all gas molecules, including the N_2 molecules, were approximated as spherical particles. This approximation significantly improves computational efficiency while maintaining the accuracy of simulations.[19] To further reduce computational cost, it was assumed that a particle is hollow with a shell thickness of 5 r_0, where r_0 is the first-neighbor distance in the FCC lattice. To maintain the spherical shape of the particle throughout the simulation, atoms within the innermost layer of the shell with a thickness of 2 r_0 were position-restrained.

Interactions between gas molecules and between gas molecules (or atoms) and particle molecules (or atoms) were described using the Lennard-Jones (L-J) 12-6 potential

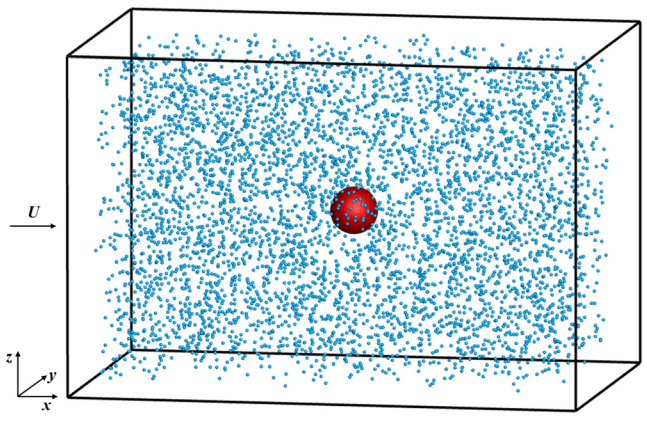

FIG. 1. Schematic of the geometry used for the molecular dynamics (MD) simulation: micro- or nano-particle (red) and a flow of gas molecules (blue).

TABLE I. L-J potential parameters.

	σ (Å)	ε/k_B[a] (K)	Source
N_2	3.652	98.4	Ref. 19
Ar	3.403	120.0	Ref. 32
He	2.600	10.2	Ref. 32
Ag	2.540	3995.4	Ref. 19
Au	4.340	290.0	Ref. 33
O(Water)	3.166	78.2	Ref. 34

[a]k_B is the Boltzmann constant.

$$U_{LJ}(r_{ij}) = \begin{cases} 4\varepsilon\left[\left(\frac{\sigma}{r_{ij}}\right)^{12} - \left(\frac{\sigma}{r_{ij}}\right)^{6}\right], & r_{ij} < r_c, \\ 0, & r_{ij} \geq r_c, \end{cases} \tag{5}$$

where ε is the depth of the potential well, σ is the finite distance at which the inter-molecule (or atom) potential is zero, r_{ij} is the distance between molecules (or atoms) i and j, and r_c is the cutoff distance, set to 2.5 σ. Quantum–mechanical effects were ignored.[31]

The cross-interaction parameters between gas and particle molecules (or atoms) are determined by the Lorentz–Berthelot mixing rules

$$\sigma_{gp} = \frac{\sigma_g + \sigma_p}{2}, \tag{6}$$

$$\varepsilon_{gp} = \sqrt{\varepsilon_g \varepsilon_p}, \tag{7}$$

where subscripts g and p denote gas molecules (or atoms) and particle molecules (or atoms), respectively. The L-J potential parameters for the gas and particle molecules or atoms used in this study are listed in Table I.

Interactions between atoms within silver and gold crystals are described using the tight-binding potential,[35] inferred from the following expression:

$$E_C = \sum_i (E_R^i + E_B^i), \tag{8}$$

where

$$E_R^i = \sum_j A_{\alpha\beta} e^{-p_{\alpha\beta}\left(\frac{r_{ij}}{r_0^{\alpha\beta}} - 1\right)}, \tag{9}$$

$$E_B^i = -\left[\sum_j \xi_{\alpha\beta}^2 e^{-2q_{\alpha\beta}\left(\frac{r_{ij}}{r_0^{\alpha\beta}} - 1\right)}\right]^{\frac{1}{2}}, \tag{10}$$

where $r_0^{\alpha\beta}$ is the first-neighbor equilibrium distance for the elemental combination $\alpha\beta$, and A, ξ, p, and q are fitting parameters. The tight-binding potential parameters for Ag and Au used in this work were taken from Ref. 35 and are listed in Table II.

TABLE II. Tight-binding potential function parameters.

	A (eV)	ξ (eV)	p	q	r_0 (Å)
Ag	0.1028	1.178	10.928	3.139	4.085
Au	0.2061	1.790	10.229	4.036	4.079

The SPC/E model was used for water molecules. This model is based on a rigid three-site representation, in which each water molecule consists of three interaction sites: one for the oxygen (O) atom and two for the hydrogen (H) atoms. The bond lengths and bond angles remained fixed during simulation. Interactions between atoms within the water model were described by Coulombic interactions for electrostatics and an L-J potential for van der Waals forces

$$U_{LJ}(r_{ij}) = 4\varepsilon\left[\left(\frac{\sigma}{r_{ij}}\right)^{12} - \left(\frac{\sigma}{r_{ij}}\right)^{6}\right] + \frac{q_i q_j}{r_{ij}}, \tag{11}$$

where q_i and q_j are an atom's Coulomb charges. The parameters for the SPC/E water model are shown in Table III.[34]

The particle-mesh Ewald (PME) method was used to compute electrostatic interactions with a Coulombic cutoff radius of 10 Å.[36] Note that computation of the L-J potential for water molecules was performed only between O atoms; interactions involving H atoms were not considered.

Simulations were performed in the (N_0+M_0, V, T) ensemble, which contains N_0 nitrogen molecules and M_0 silver atoms, gold atoms, or water molecules. The system temperature was maintained at 300 K using a Berendsen thermostat. The dimensions of the simulation box were set to be at least $7D$ in the x direction and $5D$ in the y and z directions, where D is the diameter of the particle. Periodic boundary conditions were applied in all three directions.

B. Input parameters

This study focuses on the investigation of the aerodynamic drag correction for micro- and nano-particles in air using molecular dynamics simulations. Simulations were performed for Kn of 0.5, 1, 2, 4, 6, 8, 10, 15, 20, 30, 50, and 100; particle diameters D of 30, 50, 100, and 200 nm; and relative velocities between the particles and gas flow of 3, 5, and 10 m/s. The corresponding Reynold numbers Re were in the range 7.53×10^{-4}–1.42×10^{-1}.

The time step δt was set to 1 fs for all simulations.

A quasi-steady state of the system was assumed. This state was defined as the condition in which the key physical quantities characterizing the gas–solid interaction (primarily the instantaneous drag force $F_x(t)$ in the direction of particle motion and the velocity distribution of gas molecules) fluctuate around time-averaged mean values without systematic drift, with variations arising solely from thermal noise. At this stage, collisions between the gas and solid, momentum transfer, and any potential gas adsorption reached a dynamic equilibrium, and the system no longer evolved over time. Our simulation ensured that the system enters this quasi-steady state through a two-stage process.

First, during the equilibration stage, the stationary particle was equilibrated in an NVT ensemble (a statistical ensemble that is used to study material properties under the conditions of a constant particle number N, constant volume V, and a temperature fluctuating around an equilibrium value T) using a Berendsen thermostat for a specified duration. This allowed gas molecules to achieve the Maxwell–Boltzmann velocity distribution (see Fig. 3) and stabilized the gas–solid radial distribution function (RDF) (see Fig. 2), thereby eliminating initial non-equilibrium effects. Although this state was typically achieved within 3–4 ns, we considered the first 5 ns as the relaxation period to ensure data reliability.

Second, after equilibration, the particle was set to move at the prescribed velocity. The instantaneous force $F_x(t)$ was monitored in real time, and significant fluctuations occurred initially (< 1 ns) as the gas molecules adapted to the motion of the particles. The system was considered to have reached the quasi-steady state once $F_x(t)$ started to fluctuate randomly around a constant mean value. At this stage, the average time derivative of its value approached zero. Formal data sampling was conducted for 20 ns after the quasi-steady state was established. The drag force reported in the manuscript is the time average of $F_x(t)$ during this sampling period [Eq. (12)]. The persistence of the quasi-steady state was further verified by the linearity of the time integral of $F_x(t)$ [see Fig. 4(b)].

Based on the ergodic hypothesis, all physical quantities reported in this work were obtained as long-term averages over the sampling

TABLE III. The parameters of the SPC/E water model.

O–H bond (Å)	H–O–H bond angle (°)	σ (Å)	$\varepsilon/k_B(K)$	q_O (e)	q_H (e)
1.0	109.47	3.166	78.2	−0.8476	0.4238

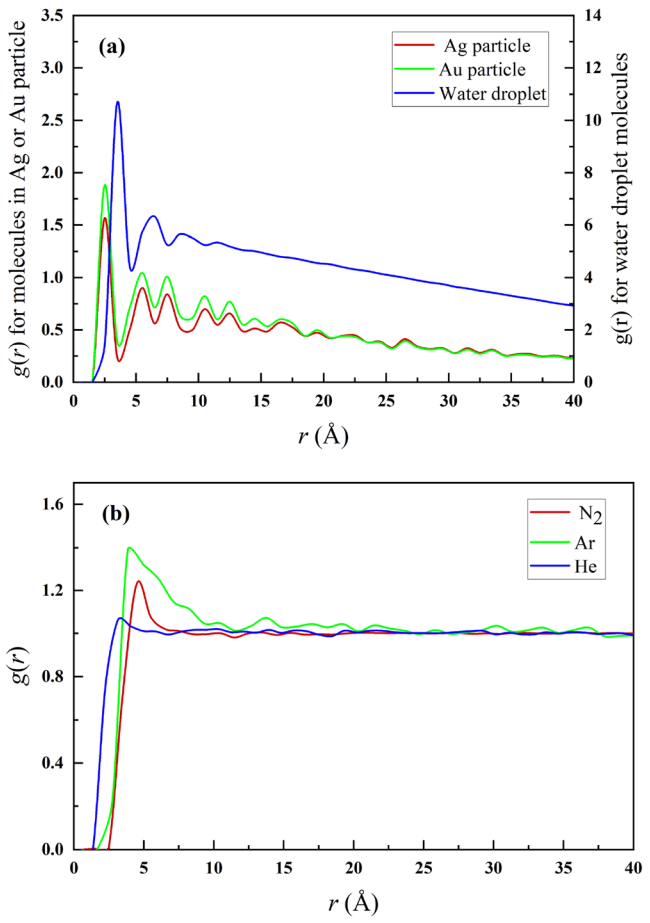

FIG. 2. The radial distribution functions $g(r)$ for molecules in a solid particle and water droplet molecules (a) and molecules of three gases (b).

duration. To ensure statistical reliability, each case was simulated three times with different initial microscopic configurations. The arithmetic mean of these three independent runs was used as the final result.

III. RESULTS AND DISCUSSION

A. Validation of the results

Before performing simulations, the radial distribution functions (or pair correlation functions) $g(r)$, which describe how the density varies as a function of distance from a reference particle, of gas molecules (or atoms) and particle molecules (or atoms), were analyzed to validate the model, and the results are shown in Fig. 2.

Figure 2(a) compares the structures of $g(r)$ for three types of molecules. The functions $g(r)$ for both silver and gold molecules are characterized by a series of distinct sharp peaks that extend to large interatomic distances, characteristic of the long-range order in an FCC crystal. The peak positions correspond precisely to the fixed distances of the first, second, and higher-order coordination shells in the FCC lattice, confirming the accuracy of the simulations in describing the crystalline structure. The gradual reduction in the amplitude of $g(r)$ with increasing distance r is primarily attributed to the finite-size effects of the particles, whose structure fundamentally differs from the periodic boundary conditions applicable to infinite bulk material. In contrast, the peak positions and line shapes of $g(r)$ for the water molecule differ markedly from those of the metallic crystal molecules. The radial distribution function of the water droplet molecules exhibits the characteristic structural features of liquids. It shows a few broad peaks within the short-range region, indicating that the ordering of water molecules is confined to short distances. The peak positions and line shapes observed in the figure correspond precisely to the molecular distribution within a spherical water droplet, reflecting the unique short-range order inherent in the disordered liquid phase.

Figure 2(b) shows the functions $g(r)$ for three types of gas molecules. The $g(r)$ profiles of N_2, Ar, and He all exhibit the characteristic short-range order and long-range disorder typical of gases. Specifically, the position of the first peak, r_{peak}, is governed primarily by the repulsive parameter σ in the intermolecular potential, while the height of the first peak, $g(r_{peak})$, correlates strongly with the depth of the potential well ε. The distinct peak positions and heights observed for the three gases align precisely with the parameters of the intermolecular potentials used in the simulations, confirming the accuracy of the model in capturing the interactions between different gas molecules.

Under equilibrium conditions in the NVT ensemble, the velocity distribution of molecules follows the Maxwell–Boltzmann distribution.[37] This distribution indicates that each Cartesian component of the velocity vector of the particle follows an independent Gaussian distribution (i.e., a normal distribution).

Figure 3(a) shows the probability distribution functions for the N_2 molecular velocity components in the x, y, and z directions at $t = 50$ ps, respectively. One can clearly see in this figure that these functions in all directions follow the standard Gaussian distributions.

Figure 3(b) shows the probability distribution functions of the N_2 molecular velocity component in the x direction at three time instants. The standard Gaussian distributions of the velocity can also be clearly observed. The same distribution in the three directions shows the isotropy of the molecular motion. Following Tobias *et al.*,[38] we can conclude that our MD simulations lead to correct results in the thermodynamic limit.

B. Aerodynamic drag and slip correction factor

In MD simulations, the force acting on a micro- or nanoparticle at any instant of time arises from discrete collisions with surrounding gas molecules. Due to the thermal fluctuations inherent in molecular motions, the instantaneous components of this force exhibit significant noise, fluctuating rapidly around mean values even when the particle moves at a constant relative velocity (as shown in Fig. 4(a) for an Ag particle with diameter $D = 50$ nm moving in N_2 at velocity $U = 5$ m/s). Consequently, the values of the mean components of this force, including its x-component (aerodynamic drag force, a macroscopic quantity), cannot be directly inferred from the components of the instantaneous force, but must be obtained from time averaging of the corresponding components of the force.

In our analysis, the aerodynamic drag force F_d acting on the particle is determined by calculating the time average of the force component along the direction of motion (x direction) as follows:

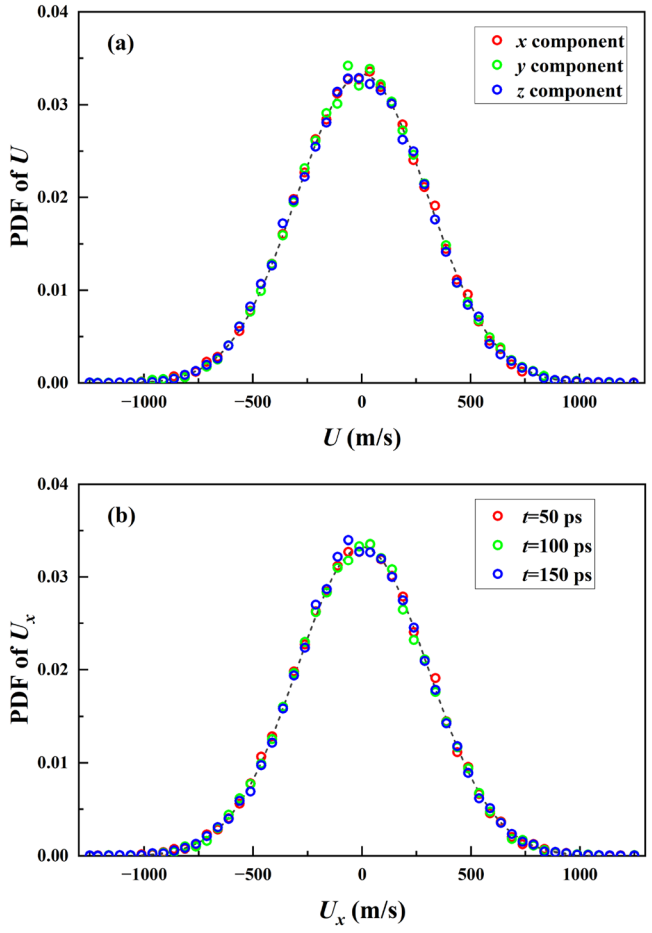

FIG. 3. Probability distribution functions (PDFs) of N_2 molecular velocity components in the x, y, and z directions at $t = 50$ ps (a), and probability distribution functions (PDF) of N_2 molecular velocity components in the x direction at three time instants (b).

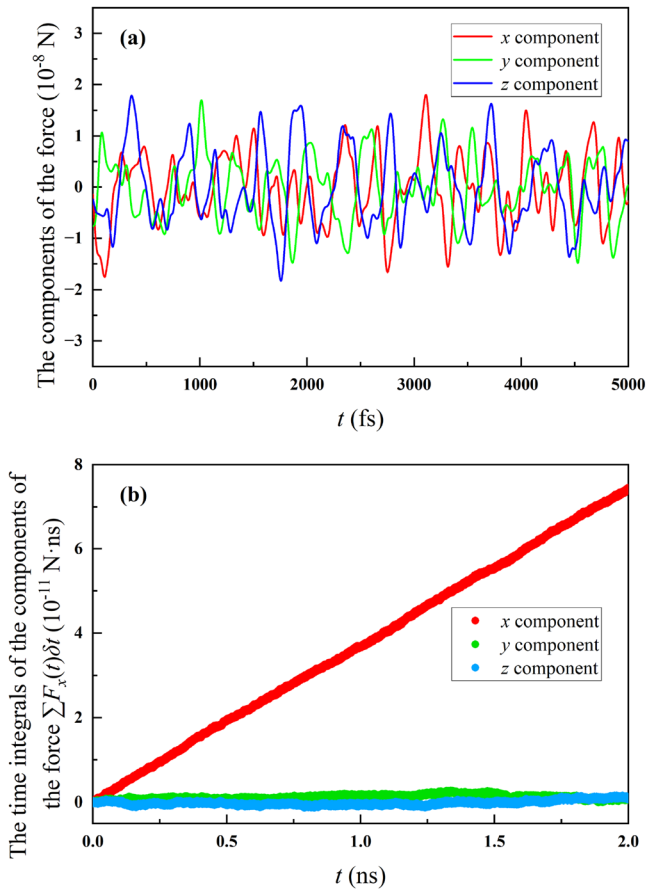

FIG. 4. The values of the components of the instantaneous force acting on an Ag particle with diameter $D = 50$ nm moving in N_2 at velocity $U = 5$ m/s (a) the integrals over time of these components of the force ($\sum_{i=1}^{N} F_{x,y,z}(t_i)\delta t$) (b).

$$F_d = \frac{1}{\Delta t}\int_{t_0}^{t_0+\Delta t} F_x(t)dt. \tag{12}$$

In the numerical code, this integral is approximated by summing the instantaneous forces $F_x(t_i)$ recorded at each time step, multiplied by the time step δt,

$$F_d \approx \frac{\sum_{i=1}^{N} F_x(t_i)\delta t}{\Delta t}, \tag{13}$$

where N is the total number of time steps and $\Delta t = N\delta t$ is the total time interval over which the averaging is performed. Other components of the drag force are calculated following the same procedure. The results of calculating the integrals over time of the three components of the force are illustrated in Fig. 4(b) for the same particle as in Fig. 4(a).

As follows from Fig. 4(b), this integral of the component of the force in the x direction is a linear function of time, whereas the values of the integrals along the y and z directions remain almost zero due to the absence of relative motion of the particle in these directions. Thus, the aerodynamic drag force, F_d, can be inferred from the slope of the curve of an integral over time of the component of the force in the x direction. For other operating conditions, curves similar to those shown in Fig. 4 were obtained. In these cases, the drag force was calculated using the same approach.

While it may seem "self-evident" from a macroscopic hydrodynamics standpoint that the drag force is present in the flow direction (x direction) and that the net transverse forces (y and z directions) are zero, this is not an *a priori* condition in a microscopic stochastic system like the one used in our MD simulation. Instead, it is a key premise that requires statistical verification, the results of which are shown in Fig. 4. The latter figure shows that the instantaneous force exhibits significant thermal noise, underscoring the necessity of time averaging. Figure 4(b) demonstrates that the time integral of the force in the x direction follows a clear linear trend, while the integrals in the y and z directions stabilize near zero over the long time interval. This directly verifies the isotropy and absence of bias in our simulated system, ruling out nonphysical drifts caused by boundary conditions, initial configurations, or algorithmic artifacts.

In fact, Fig. 4(b) shows the reliability of our drag force calculation: using the slope method [i.e., the slope of the curve in Fig. 4(b)], we extract the average drag force using Eqs. (12) and (13). This figure provides an intuitive and transparent data foundation for this method, enhancing the credibility of our results. It is standard practice in the field of MD simulations to present data such as that shown in Fig. 4. The presentation of raw force signals and their statistical convergence behavior are widely used in MD studies. This helps readers to assess the quality of the simulation and the adequacy of sampling. Although Fig. 4 may appear to be simple, it is crucial to the validation of simulation reliability, clarification of data processing logic, and enhancing the rigor of the paper.

To investigate the effects of particle diameter D and velocity U at various Kn (estimated based on the free-molecular path in the ambient gas) on the drag force, the values of the slip correction factor C [used in Expression (2)] of Ag particles in gas N_2 for various particle velocities U, diameters D, and Kn were calculated. The results are shown in Fig. 5 in the form of plots of C vs Kn for seven combinations of U and D. As follows from Fig. 5, the dependencies of C on D and U are very weak for Kn in the range 0.5–100. In all cases, C increases with increasing Kn. The same behavior of C was observed for other combinations of particles and gases. Therefore, our analyses will focus on particles with diameter $D = 50$ nm moving with velocity $U = 5$ m/s to improve computational efficiency and allow systematic comparison of drag characteristics in various gas–particle combinations.

The slip correction factors C vs Kn for five particle–gas combinations are shown in Fig. 6. As in the cases presented in Fig. 5, the values of C shown in Fig. 6 increase with increasing Kn. In all the cases shown in Fig. 6, C increases linearly with Kn. The values of C at fixed Kn, however, vary significantly depending on the particle/gas combination. For example, the values of C for Ag–N_2 and Au–N_2 are nearly identical across the whole range of Kn under consideration. Higher values of C are predicted for the water–N_2 and Ag–He combinations. The highest values of C are predicted for the Au–He combination. The latter result agrees well with the experimental results reported by Millikan.[6] Millikan[6] claimed that C depends solely on Kn and does not depend on gas and particle materials. In contrast to the conclusion drawn by Millikan,[6] our results show that the dependence of C on the

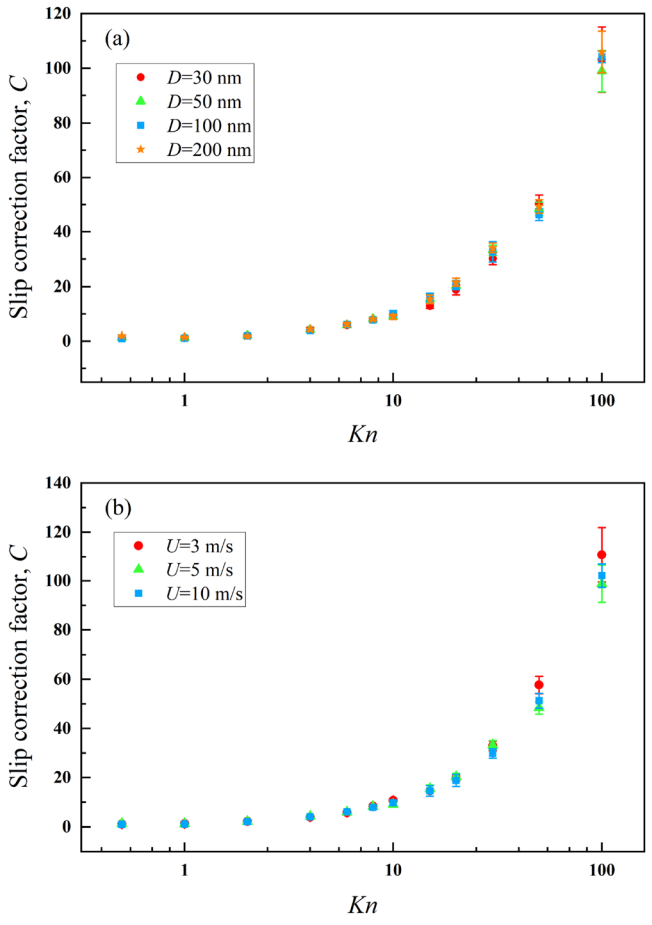

FIG. 5. The slip correction factor for an Ag particle in N_2 gas vs *Kn* for four particle diameters *D* and $U = 5$ m/s (a) and for three particle velocities *U* and $D = 50$ nm (b). The logarithmic scale of *Kn* is used.

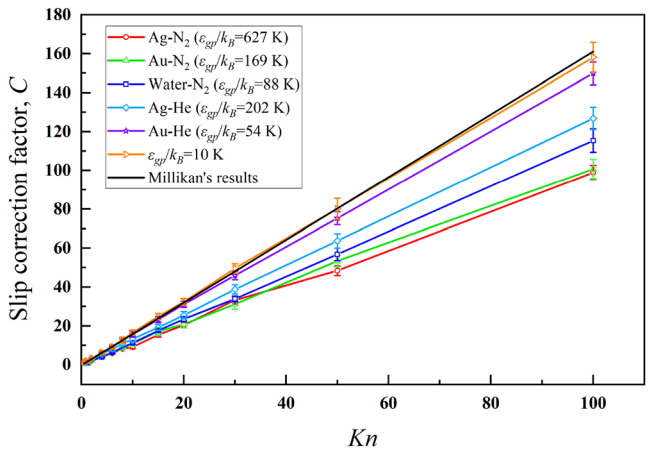

FIG. 6. The slip correction factor *C* vs *Kn* for five particle–gas combinations, an artificial combination with $\varepsilon_{gp}/k_B = 10$ K, and inferred from Millikan's experiments. The linear scale of *Kn* is used.

particle/gas combination is clearly visible and cannot be ignored. Note that the results obtained by Millikan[6] are consistent with the theoretical solution presented by Epstein[13] for $Kn > 1$.

Epstein's theory is based on a rigid-body collision model and assumes that the number density of gas molecules colliding with the particle at its surface equals the ambient gas number density. However, at micro- and nano-scales, inelastic collisions are often expected. Also, gas molecules can be adsorbed on the surface of the particle, leading to a local gas number density significantly higher than that under ambient conditions.[16,18] The analysis of this effect is one of the focuses of our investigation.

The local gas number density is controlled by both particle–gas and gas–gas interactions. The interaction strength ε_{gp} between particle and gas molecules serves as the foundation: only when this interaction is sufficiently strong can gas molecules be captured in the vicinity of the particle surface, initially forming a local molecular enrichment region. Without this prerequisite, gas molecules remain in a free diffusion state, and the local number density cannot be significantly higher than the ambient density. Gas–gas interaction acts as an amplifying factor in enhancing the local density. The high-density region significantly increases the probability of interaction between incoming gas molecules and those present in the region. After the initial high-density region is formed via gas–particle interactions, the probability of interactions between incoming gas molecules and those already present in the region increases substantially. ε_g directly determines the capture efficiency of these interactions: a larger ε_g makes it easier for molecules to form transient clusters or local aggregates, thereby reducing molecular escape and further increasing the local number density. Conversely, gas molecules with a smaller ε_g, even if they enter a high-density region, are less likely to be captured by other molecules, readily diffuse away from the region, and cannot sustain a stable high-density layer.

For systems with weak interactions (e.g., Au–He with $\varepsilon_{gp}/k_B \approx 54$ K and Ag–He with $\varepsilon_{gp}/k_B \approx 202$ K, and a virtual combination with $\varepsilon_{gp}/k_B \approx 10$ K), the particle's capacity to capture gas molecules is limited, and the local number density near the particle surface N_{wall} remains close to that in the ambient gas (N_{env}) across all values of *Kn* under consideration. This is illustrated in Fig. 7(a). The plots of the molecular number density vs the distance to the particle surface for the Ag–N_2 combination (with an Ag particle diameter of 50 nm) and 12 values of the Knudsen number are shown in Fig. 7(b). As can be clearly seen from the latter figure, the particle surface affects the molecular number density only at distances less than 10 Å. The distributions of molecular number density for other combinations of particle and gas molecules were similar to those shown in Fig. 7(b).

In such cases, the Epstein theory[13] assumptions hold, and the values of *C* obtained in this work agree with its predictions. In contrast, for stronger interactions (e.g., Ag–N_2 with $\varepsilon_{gp}/k_B \approx 627$ K), the adsorption of gas molecules on the surface of the particle is significantly enhanced, resulting in $N_{wall}/N_{env} \gg 1$. In this case, the actual aerodynamic drag exceeds Epstein's theoretical predictions, leading to significantly lower *C* values, as demonstrated in our paper. This observation is consistent with the findings of Liu *et al.*[18]

The relatively strong particle–gas interaction for Ag–He when $\varepsilon_{gp}/k_B \approx 202$ K meets the prerequisite conditions for forming an initial high-density region. However, the intermolecular potential well depth of He is small ($\varepsilon_g/k_B \approx 10.2$ K). This weak gas–gas interaction makes it difficult for other He molecules in the high-density region to capture

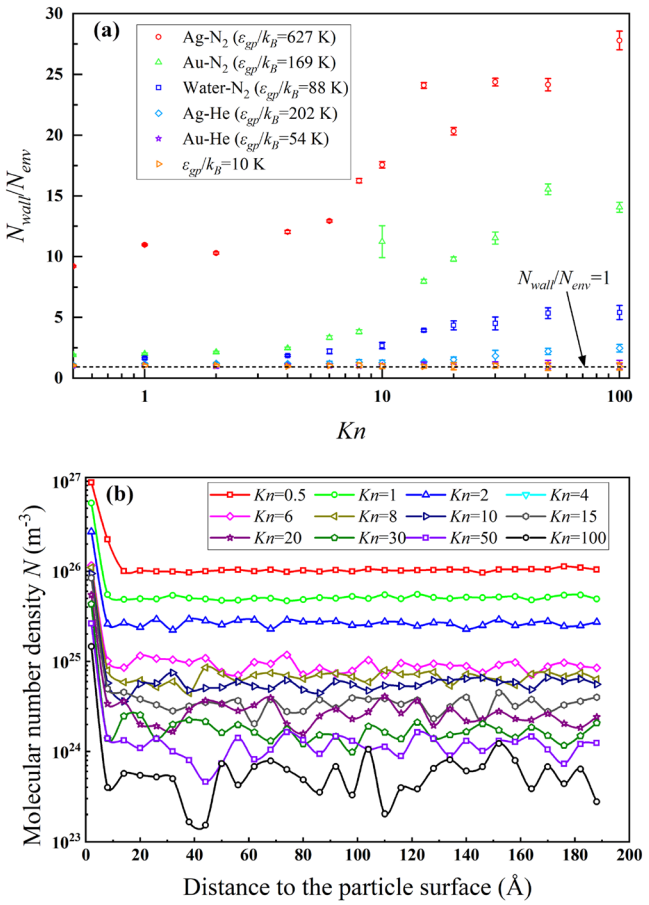

FIG. 7. The ratio of the gas number density near the particle and the average gas number density vs *Kn* for five particle–gas combinations and an artificial combination with $\varepsilon_{gp}/k_B = 10$ K (a). The molecular number density vs the distance to the particle surface for the Ag–N_2 combination (with an Ag particle diameter of 50 nm) and 12 values of the Knudsen number (b).

He molecules entering the region. Thus, the increased probability of interaction does not translate into further increase in N_{wall}/N_{env} which remains at a relatively low level (approximately 1.5–2).

Note that although the values of ε_{gp}/k_B for Au–N_2 (approximately 169 K) and water-N_2 (approximately 88 K) are lower than those for Ag–He (approximately 202 K), the former show higher values of N_{wall}/N_{env} and lower values of *C*. This phenomenon arises because the number of molecules adsorbed near the particle surface depends not only on the strength of gas–particle interactions but also on the intermolecular potential between gas molecules. As discussed previously, stronger intermolecular potentials facilitate tighter packing and increase local number density for the same adsorption capacity, whereas weaker potentials promote molecular dispersal.

To account for the coupled effects of gas–particle and gas–gas interactions on the slip correction factor, a comprehensive potential depth parameter ε_{ggp} is proposed

$$\varepsilon_{ggp} = \sqrt[3]{\varepsilon_g \varepsilon_g \varepsilon_p} = \varepsilon_g^{2/3} \varepsilon_p^{1/3}. \quad (14)$$

The values of ε_{ggp}/k_B for the systems studied are as follows: 338 K for Ag–N_2, 140 K for Au–N_2, 91 K for water–N_2, 74 K for Ag–He, and 31 K for Au–He. These values further support the foregoing discussions. Further analysis indicates that when $\varepsilon_{ggp}/k_B \leq 31$ K or ≥ 140 K, the value of *C* stabilizes near upper or lower critical values, and the influence of varying gas and particle materials becomes negligible. However, when $31\text{ K} < \varepsilon_{ggp}/k_B < 140$ K, the specific properties of the gas–particle combinations must be taken into account.

Note that, in gases at Kn $\gg 1$, traditional free-molecular flow theory is based on the assumption that gas molecules move independently, interacting with the particle surface only through single collisions; intermolecular interactions are ignored. However, in actual micro- or nano-scale flows, a localized high-density gas layer can be present near the particle surface, even at elevated Kn (cf. Fig. 7), resulting from adsorption or clustering effects induced by strong gas–particle attractive forces. Within this region, the intermolecular spacing of the gas is significantly reduced. The average distance between gas molecules can approach or even fall below the range of their Lennard-Jones potential, making gas–gas interactions non-negligible. Under these conditions, ε_g influences two key processes: formation of the near-wall gas structure and alteration of momentum transfer pathways.

During the formation of the near-wall gas structure, strong mutual interactions between gas molecules help to stabilize the adsorption layer, local molecular packing, and consequently further the local number density. During the alteration of momentum transfer pathways, gas molecules undergo multiple collisions near the particle surface (including both gas–gas and gas–particle collisions), and momentum transport from the bulk flow to the particle surface is no longer reliant solely on single impacts. It may instead occur through localized continuum-like behavior, which enhances the effective drag force. Therefore, consideration of only ε_{gp} (gas–particle interaction) is insufficient to capture this coupled effect. The introduction of the comprehensive parameter ε_{ggp} essentially characterizes, via a geometric mean, the synergistic effect between the gas–gas cohesion tendency and the gas–particle adsorption capability. Its physical significance lies in the fact that high ε_g enhances the effect of strong gas–particle interactions on the near-wall gas density and the resulting drag force.

C. Slip parameter

To further investigate the differences in slip effects among various gas–particle systems, the slip parameter *A*, used to correct the Stokes drag force [see Expression (4)], was investigated. The plots of *A* vs *Kn* for six particle-gas combinations, an artificial combination with $\varepsilon_{gp}/k_B = 10$ K, and inferred from Millikan's experiments are shown in Fig. 8.

As follows from Fig. 8, although *A* in all cases increases with *Kn*, the values of this parameter for various particle–gas combinations turned out to be quite different.

For the Ag–N_2, Au–N_2, and Ag–Ar combinations, the values of *A* were very close throughout the range *Kn* = 0.5–100, increasing from approximately 0.1 to around 1.0 with increasing *Kn* before stabilizing at $A \approx 1$. For the water–N_2 and Ag–He combinations, the values of *A* were higher than those for the Ag–N_2, Au–N_2, and Ag–Ar combinations for all *Kn* considered. They increased from approximately 0.4 and 0.5 to approximately 1.1 and 1.2 with increasing *Kn* before stabilizing at $A \approx 1.1$ and $A \approx 1.2$, respectively. For the Au–He

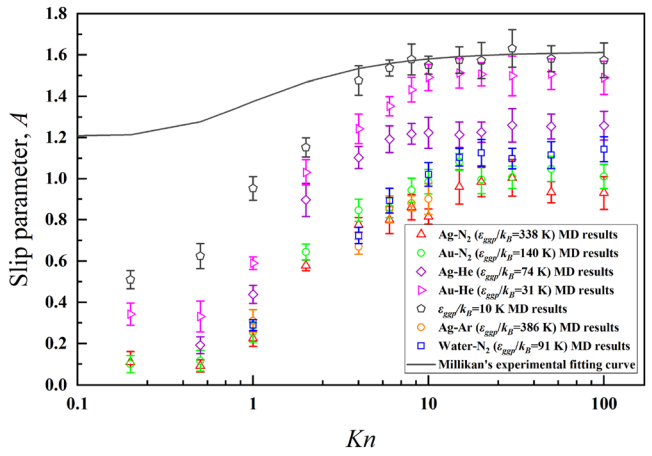

FIG. 8. The plots of A vs Kn for six particle–gas combinations, an artificial combination with $\varepsilon_{gp}/k_B = 10$ K, and inferred from Millikan's experiments.

combination, the predicted values of A were even higher, stabilizing at $A \approx 1.5$ for $Kn \approx 100$.

Note that in most previous studies,[6,11,39] it was assumed that A is almost independent of particle–gas combinations, which contradicts our findings. On the other hand, our results are consistent with those of Hutchins *et al.*,[9] who demonstrated that differences in molecule–surface interactions lead to variations in the drag correction coefficient. As follows from our analysis, the importance of considering the effect of particle–gas combinations depends on the potential depth parameter, ε_{ggp}/k_B. When $\varepsilon_{ggp}/k_B \leq 31$ K (e.g., the Au–He combination), $N_{wall}/N_{env} \approx 1$ (Fig. 7), and A approaches approximately 1.5 at $Kn \gg 1$. This is consistent with Epstein's prediction and experimental observations.[6–9] As ε_{ggp}/k_B increased, the value of A for these Kn gradually decreased. This can be attributed to the following two effects.

First, an increase in ε_{ggp}/k_B leads to a change in the nature of gas–particle collisions. Elastic collisions for small ε_{ggp}/k_B become inelastic for large ε_{ggp}/k_B. The latter enhances momentum transfer between gas molecules and the particle, thus increasing aerodynamic drag and decreasing the slip parameter A.

Second, strong gas–particle interactions during inelastic collisions lead to the capture of gas molecules at the particle surface. This leads to an increase in the local number density of gas molecules (i.e., $N_{wall}/N_{env} > 1$). For large Kn, this effect leads to an increase in the aerodynamic drag above Epstein's theoretical prediction, thus reducing the value of A.

As follows from our analysis, the slip parameter A depends not only on Kn but is also highly sensitive to the physical properties of the gas and particle. Note that A is insensitive to the physical state of the particle (solid or liquid), but is primarily controlled by the strength of intermolecular interactions between the molecules (or atoms) of the particle and the gas molecules (or atoms). The value of A was shown to be controlled by a newly introduced parameter ε_{ggp}/k_B with its critical thresholds near 31 and 140 K. The following approximation of the results of our calculations is suggested:

$$A = \left[0.478 + 1.160e^{\left(-\frac{0.924}{Kn}\right)}\right] f(\varepsilon_{ggp}/k_B), \tag{15}$$

$$f(\varepsilon_{ggp}/k_B) = \begin{cases} 0.261 + 0.739e^{(-0.0186\varepsilon_{ggp}/k_B)}, & Kn \leq 1, \\ 0.556 + 0.444e^{(-0.0152\varepsilon_{ggp}/k_B)}, & 1 < Kn \leq 10, \\ 0.623 + 0.377e^{(-0.0124\varepsilon_{ggp}/k_B)}, & Kn > 10. \end{cases} \tag{16}$$

To illustrate the application of Formula (15) to the analysis of real-life experimental data, we compared its predictions with the results of measurements of the slip parameter A of polystyrene latex (PSL) particles with diameters of 19.9, 100.7, and 269.0 nm in air over a Kn range 0.5–83, obtained by Kim *et al.*[10] Since the parameter ε_p/k_B for PSL has not been measured, to the best of our knowledge, we used it as a fitting parameter in our analysis. It was found that $\varepsilon_p/k_B = 3$ K leads to a reasonable agreement between the predictions of Formula (15) and the experimental data for $Kn > 10$ as illustrated in Fig. 9. The air was approximated as pure nitrogen since the volume fraction of this gas exceeded 70 %.

The solid red curve in Fig. 9 shows the results of the calculations averaged over three runs. The shaded area shows the 95% confidence band (when the same simulation conditions and procedures are repeated multiple times, 95% of the predicted values of A are expected to be within this range). As follows from this figure, the 95% confidence band overlaps with the observed values of A within error bars at $Kn > 10$.

The predictions of Epstein's model[13] for $Kn \gg 1$ and for diffuse (short dashes) and specular (long dashes) reflections are shown in the same Fig. 9. In real-life cases, a mixture of diffuse and specular reflections is expected. As follows from Fig. 9, although Epstein's model can predict the observed values of A reasonably well, it cannot predict the observed decrease in A. This is related to the main limitation of that model and that it does not consider the differences between the ambient gas density and its density near the particle surface. The closeness of the prediction of Epstein's model and the model described in the paper was to be expected since $\varepsilon_p/k_B = 3$ K is less than the threshold value of 31 K discussed earlier.

Note that diffuse and specular reflections are characterized by the tangential momentum accommodation coefficient σ_t. $\sigma_t = 1$ corresponds to fully diffuse reflection, while $\sigma_t = 0$ corresponds to perfectly specular reflection. In the simulations, the results of which are

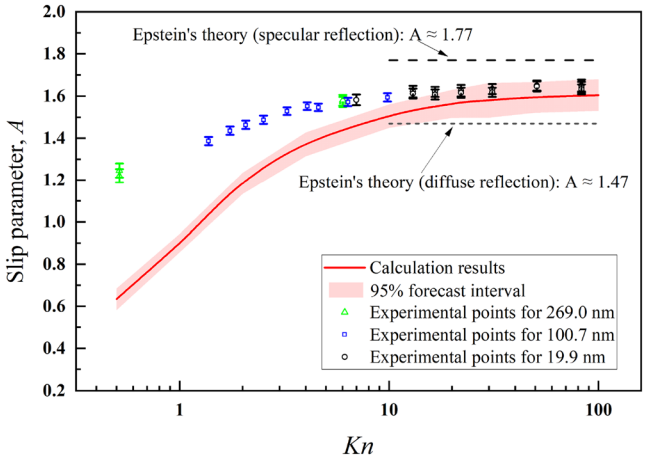

FIG. 9. Comparison of slip parameter A for the PSL–N_2 combination: simulation vs experiment.

presented in our paper, the diffuse or specular reflections are not explicitly separated. They are inferred from the realistic gas–particle interaction potential (Lennard-Jones potential) and the thermodynamic state of the particle surface. Our simulation results implicitly captured this mixed reflection mechanism through the decomposition of the total drag force into its normal and tangential components.

The predicted percentages of the normal component in the drag force vs Kn for Ag particles and two gases (N_2 and He) are shown in Fig. 10. As follows from this figure, the tangential component of this force constitutes 30%–40% of the total drag at $Kn < 1$, which is consistent with a largely diffuse reflection for these Kn. At $Kn > 10$, this contribution decreases to below 15%, indicating a transition toward more specular-like reflection as gas rarefaction increases.

The significant decrease predicted in the contribution of the tangential force with increasing Kn follows from the changes in σ_t. In the continuum and slip flow regimes ($Kn < 1$), the substantial contribution of the tangential force indicates a high degree of tangential momentum exchange, consistent with a predominantly diffuse reflection mechanism ($\sigma_t \to 1$). This is related to the fact that frequent gas–gas collisions near the surface facilitate the randomization of molecular trajectories upon reflection.

However, in the transition and free-molecular flow regimes ($Kn > 10$), the tangential force becomes negligible, suggesting that the reflected molecules largely retain their incident tangential momentum relative to the surface, corresponding to a more specular reflection ($\sigma_t \to 0$). In this case, the molecules impinging on the surface undergo few, if any, collisions with other gas molecules before and after interaction with the particle, thus reducing the randomization of their tangential velocity components.

Regarding the notable discrepancies between the model predictions and the experimental data for $Kn < 10$, clearly seen in Fig. 9, we can tentatively attribute these to the considerable scatter of the experimental data for these Kn. According to some observations (e.g., Ref. 14), in this range of Kn, A decreases (rather than increases, e.g., Ref. 39) with increasing Kn.

In Ref. 14, the slip parameters for silica microspheres (with diameters of 1, 2, 4, and 8 μm) and glass microspheres (with diameters of 45 μm) in dry air were studied. The study presented in Ref. 39, on the other hand, focused on the slip parameters of oil droplets in nine gases: air, argon, helium, hydrogen, methane, ethane, isobutane, nitrous oxide, and carbon dioxide.

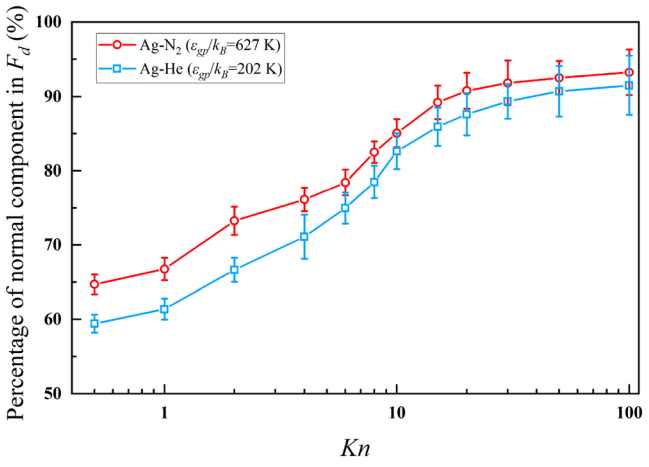

FIG. 10. The percentage of the normal component in F_d vs Kn for Ag particles and two gases (N_2 and He).

The experimental errors in the slip parameters of PSL particles[10] are notably smaller than those of silica and glass particles.[14] This is attributed to the certified NIST reference material status of PSL particles, which ensures high dimensional accuracy (with an uncertainty of 0.5 %–0.63 %) and excellent dispersion. The drag force on PSL particles was determined via electrical mobility measurements using nano-differential mobility analyzers (NDMA), a method characterized by high precision, large sample size, and a short error propagation chain. In contrast, silica and glass microspheres exhibit a significant size variation (3 %–5 %) and a tendency to agglomerate. The drag force for these was indirectly derived from settling velocity measurements made using laser Doppler velocimetry (LDV), a process involving multiple conversion steps that accumulate errors. Additional uncertainties arise from single-particle detection limitations and gas pressure measurement errors of 1 %–3 %, further increasing the overall uncertainty.

IV. CONCLUSIONS

The effects of Knudsen numbers, particle sizes, relative particle velocities, and particle and gas properties on the drag force of micro- and nano-particles moving in gas were investigated using the molecular dynamics approach. These are the main findings of our analysis.

- The slip correction factor C and the slip parameter A are shown to depend not only on the value of Kn, as commonly assumed, but also on the physical properties of gases and particles. Quantitative analysis of the ratio between local (near the particle surface) and ambient gas number densities showed that increased gas–particle interactions at micro- and nano-scales lead to an increase in the local gas number density. This increase in the local gas density is shown to lead to an increase in the drag force.
- A comprehensive potential depth parameter, ε_{ggp}, is introduced to take into account gas–particle and gas–gas interactions. This parameter allowed us to provide a unified framework for interpreting slip correction behavior across different particle–gas combinations. Two critical thresholds are identified: $\varepsilon_{ggp}/k_B \approx 31$ and 140 K. For $\varepsilon_{ggp}/k_B < 31$ K and $\varepsilon_{ggp}/k_B > 140$ K, the slip parameter was shown to remain stable and independent of the particle–gas combinations, while between these thresholds, the effects of these combinations must be taken into account.
- A predictive universal approximation of the slip parameter A as a function of ε_{ggp} and Kn is suggested and compared with the available experimental data. The prediction of this approximation was shown to be in good agreement with experimental data referring to the drag forces experienced by polystyrene latex (PSL) particles in a nitrogen atmosphere at $Kn > 10$, but not for smaller Kn.

ACKNOWLEDGMENTS

The authors gratefully acknowledge the financial support of the National Natural Science Foundation of China (Grant No. 82361138571) (contribution by Ning-Ning Liu and Bing-Yang Cao) and the Russian Science Foundation (Project No. 24-45-00012, https://rscf.ru/project/24-45-00012/) (contribution by S.S. Sazhin).

AUTHOR DECLARATIONS

Conflict of Interest

The authors have no conflicts to disclose.

Author Contributions

Ning-Ning Liu: Conceptualization (equal); Data curation (equal); Formal analysis (equal); Investigation (equal); Methodology (equal); Resources (equal); Software (equal); Validation (equal); Visualization (equal); Writing – original draft (equal); Writing – review & editing (equal). **Bing-yang Cao:** Conceptualization (equal); Investigation (equal); Methodology (equal); Project administration (equal); Resources (equal); Software (equal); Supervision (equal); Writing – original draft (equal); Writing – review & editing (equal). **Sergei Sazhin:** Conceptualization (equal); Funding acquisition (equal); Investigation (equal); Project administration (equal); Supervision (equal); Writing – original draft (equal); Writing – review & editing (equal).

DATA AVAILABILITY

The data that support the findings of this study are available from the corresponding authors upon reasonable request.

REFERENCES

[1]M. J. Breddan and R. E. Wirz, "Electrospray plume evolution: Influence of drag," J. Aerosol Sci. **167**, 106079 (2023).
[2]H. Zhuo, C. He, C. Yang, X. Jiang, F. Li, X. Yang, H. Yang, T. Yong, Z. Liu, Y. Ma, L. Nie, G. Liao, and T. Shi, "Integration of acoustic, optical, and electrical methods in picoliter droplet microfluidics for rare particles enrichment," Commun. Eng. **4**(1), 86 (2025).
[3]D. Westmeier, D. Solouk-Saran, C. Vallet, S. Siemera, D. Doctera, H. Götzd, L. Männb, A. Hasenbergb, A. Hahlbrocka, K. Erlerb, C. Reinhardte, O. Schillingf, S. Beckera, M. Gunzerb, M. Hasenbergb, S. K. Knauerc, and R. H. Stauber, "Nanoparticle decoration impacts airborne fungal pathobiology," Proc. Natl. Acad. Sci. U. S. A. **115**(27), 7087–7092 (2018).
[4]E. Cunningham, "On the velocity of steady fall of spherical particles through fluid medium," Proc. R. Soc. London, Ser. A **83**(563), 357–365 (1910).
[5]M. Knudsen and S. Weber, "Luftwiderstand gegen die langsame bewegung kleiner kugeln," Ann. Phys. **341**(15), 981–994 (1911).
[6]R. A. Millikan, "Coefficients of slip in gases and the law of reflection of molecules from the surfaces of solids and liquids," Phys. Rev. **21**(3), 217 (1923).
[7]M. D. Allen and O. G. Raabe, "Re-evaluation of Millikan's oil drop data for the motion of small particles in air," J. Aerosol Sci. **13**(6), 537–547 (1982).
[8]M. D. Allen and O. G. Raabe, "Slip correction measurements of spherical solid aerosol particles in an improved Millikan apparatus," Aerosol Sci. Technol. **4**(3), 269–286 (1985).
[9]D. K. Hutchins, M. H. Harper, and R. L. Felder, "Slip correction measurements for solid spherical particles by modulated dynamic light scattering," Aerosol Sci. Technol. **22**(2), 202–218 (1995).
[10]J. H. Kim, G. W. Mulholland, S. R. Kukuck, and D. Y. Pui, "Slip correction measurements of certified PSL nanoparticles using a nanometer differential mobility analyzer (nano-DMA) for Knudsen number from 0.5 to 83," J. Res. Natl. Inst. Stand. Technol. **110**(1), 31 (2005).
[11]H. Jung, G. W. Mulholland, D. Y. Pui, and J. H. Kim, "Re-evaluation of the slip correction parameter of certified PSL spheres using a nanometer differential mobility analyzer (NDMA)," J. Aerosol Sci. **51**, 24–34 (2012).
[12]H. Jung, K. Han, G. W. Mulholland, D. Y. H. Pui, and J. H. Kim, "Effect of the surface energy of particle materials on the accommodation of gas molecules to the particle surfaces," J. Aerosol Sci. **65**, 42–48 (2013).
[13]P. S. Epstein, "On the resistance experienced by spheres in their motion through gases," Phys. Rev. **23**(6), 710 (1924).
[14]A. B. Jakobsen, J. Merrison, and J. J. Iversen, "Laboratory study of aerosol settling velocities using Laser Doppler velocimetry," J. Aerosol Sci. **135**, 58–71 (2019).
[15]C. Liu and H. Wang, "Nanoparticles in dilute gases: Fundamental equivalence between momentum accommodation and surface adsorption," Phys. Rev. E **99**(4), 042127 (2019).
[16]W. Liu, J. W. G. Xia, and Z. Li, "Thermophoresis of nanoparticles in the transition regime," Phys. Fluids **35**(8), 083316 (2023).
[17]S. Luo, J. Wang, S. Yu, G. Xia, and Z. Li, "Shear lift forces on nanocylinders in the free molecule regime," J. Fluid Mech. **846**, 392–410 (2018).
[18]W. Liu, K. Zhang, J. Wang, and G. Xia, "Simulation study of drag force characteristics of nanoparticles in transition regime," Acta Phys. Sin. **73**(7), 075101 (2024).
[19]Z. Li and H. Wang, "Gas-nanoparticle scattering: A molecular view of momentum accommodation function," Phys. Rev. Lett. **95**(1), 014502 (2005).
[20]H. Jin, N. Liu, X. Ku, and J. Fan, "Preferential frequency and size effect of the Brownian force acting on a nanoparticle," J. Fluid Mech. **828**, 648–660 (2017).
[21]Z. Li and H. Wang, "Drag force, diffusion coefficient, and electric mobility of small particles. II. Application," Phys. Rev. E **68**(6), 061207 (2003).
[22]H. Yu, H. Gu, Z. Sun, Y. Zhou, J. Chen, and Y. Li, "Experimental and numerical study on the gravitational deposition and coagulation of aerosols," Front. Energy Res. **10**, 840503 (2022).
[23]G. H. Spasov, R. Rossi, A. Vanossi, C. Cottini, and A. Benassi, "A critical analysis of the CFD-DEM simulation of pharmaceutical aerosols deposition in upper intra-thoracic airways: Considerations on air flow," Comput. Biol. Med. **170**, 107948 (2024).
[24]M. M. Rahman, M. Zhao, M. S. Islam, K. Dong, and S. C. Saha, "Aerosol particle transport and deposition in upper and lower airways of infant, child and adult human lungs," Atmosphere **12**(11), 1402 (2021).
[25]A. T. John and A. Tricoli, "Flame assisted synthesis of nanostructures for device applications," Adv. Phys. X **7**(1), 1997153 (2022).
[26]J. Y. Lai, K. C. Lin, and A. Violi, "Biodiesel combustion: Advances in chemical kinetic modeling," Prog. Energy Combust. Sci. **37**(1), 1–14 (2011).
[27]Y. Ren, J. Cai, and H. Pitsch, "Theoretical single-droplet model for particle formation in flame spray pyrolysis," Energy Fuels **35**(2), 1750–1759 (2021).
[28]Y. Tang and B. Guo, "Computational fluid dynamics simulation of aerosol transport and deposition," Front. Environ. Sci. Eng. China **5**(3), 362–377 (2011).
[29]C. Xuan, W. Liang, B. He, and B. Wen, "Active control of particle position by boundary slip in inertial microfluidics," Phys. Rev. Fluids **7**(6), 064201 (2022).
[30]X. Du, Z. Zhuo, X. Li, X. Li, M. Li, J. Yang, Z. Zhou, W. Gao, Z. Huang, and L. Li, "Design and simulation of aerosol inlet system for particulate matter with a wide size range," Atmosphere **14**(4), 664 (2023).
[31]S. Sazhin, *Droplets and Sprays: Simple Models of Complex Processes* (Springer, 2022).
[32]G. L. Pollack, "Extension of the law of corresponding states to rare-gas solids," Phys. Rev. A **2**(1), 38 (1970).
[33]F. Delogu, "Thermodynamic stability of nanometre-sized Cu_3Au systems," Nanotechnology **22**(15), 155704 (2011).
[34]H. J. C. Berendsen, J. R. Grigera, and T. P. Straatsma, "The missing term in effective pair potentials," J. Phys. Chem. **91**(24), 6269–6271 (1987).
[35]F. Cleri and V. Rosato, "Tight-binding potentials for transition metals and alloys," Phys. Rev. B **48**(1), 22 (1993).
[36]U. Essmann, L. Perera, M. L. Berkowitz, T. Darden, H. Lee, and L. G. Pedersen, "A smooth particle mesh Ewald method," J. Chem. Phys **103**(19), 8577–8593 (1995).
[37]P. Todorov and D. Bloch, "Testing the limits of the Maxwell distribution of velocities for atoms flying nearly parallel to the walls of a thin cell," J. Chem. Phys. **147**(19), 194202 (2017).
[38]D. J. Tobias, G. J. Martyna, and M. L. Klein, "Molecular dynamics simulations of a protein in the canonical ensemble," J. Phys. Chem. **97**, 12959–12133 (1993).
[39]D. J. Rader, "Momentum slip correction factor for small particles in nine common gases," J. Aerosol Sci. **21**(2), 161–168 (1990).